Journal of Cleaner Production 276 (2020) 124156

Contents lists available at ScienceDirect

Journal of Cleaner Production

journal homepage: www.elsevier.com/locate/jclepro

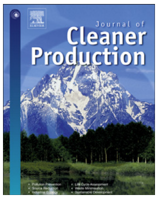

Dynamic insights into combustion drivers and responses of water hyacinth: Evolved gas and ash analyses

Hongyi Huang [a], Jingyong Liu [a, *], Hui Liu [a], Jinwen Hu [a], Fatih Evrendilek [b]

[a] *Guangdong Key Laboratory of Environmental Catalysis and Health Risk Control, School of Environmental Science and Engineering, Guangdong University of Technology, Guangzhou, 510006, China*

[b] *Department of Environmental Engineering, Bolu Abant Izzet Baysal University, Bolu, 14052, Turkey*

ARTICLE INFO

Article history:
Received 14 May 2020
Received in revised form
4 September 2020
Accepted 7 September 2020
Available online 11 September 2020

Handling editor: Cecilia Maria Villas Bôas de Almeida

Keywords:
Water hyacinth
Bioenergy
Thermal conversion
Gas emission
Ash deposition

ABSTRACT

Non-food biomass feedstocks owing to their advantages have come to the forefront as the efforts have been intensified to develop cleaner energy sources and technologies in the face of global climate change. This study aimed to dynamically characterize the combustion drivers and responses including the gas emission and ash deposition risks for roots (WHR) and stems and leaves (WHSL) of water hyacinth. Their combustion processes consisted of the four sequential stages of the water evaporation, the combustions of volatiles and fixed carbon, and the degradation of minerals. The WHR combustion had a higher total heat release (2140.6–4226.7 J/g) than did the WHSL combustion (1255.6–3110.6 J/g). In terms of the Flynn-Wall-Ozawa method, the average activation energy was estimated at 167.42 and 172.41 kJ/mol for WHR and WHSL, respectively. The reaction mechanisms of the volatiles and fixed carbon combustion stages were best elucidated by the F1 ($f(\alpha) = 1\text{-}\ \alpha$) and F3 ($f(\alpha) = (1\text{-}\ \alpha)^3$) models for WHR and the F3 ($f(\alpha) = (1\text{-}\ \alpha)^3$) and F1.5 ($f(\alpha) = (1\text{-}\ \alpha)^{1.5}$) models for WHSL, respectively. CO_2 was the main evolved gas for both WHR and WHSL and exhibited the fastest response to temperature. Evolved S-containing gases (SO_2 and COS) (0.13% for WHR and 0.12% for WHSL) were extremely low. The WHSL ash had a higher risk of slagging and fouling than did the WHR ash. Our findings can provide insights into the cleaner and optimal production of the water hyacinth combustion.

1. Introduction

Population and consumption growth has increased the world energy consumption, 80% of which is still realized through the burning of fossil fuels (Chen et al., 2015). The aggregate impact of the fossil-fuel dependency of nations has emerged to the humankind in the form of global climate change. Recently, efforts have been intensified about how to develop cleaner energy sources and technologies. In particular, owing to their advantages such as carbon neutralization, renewability, low pollutants, and non-rivalry with the scarce croplands, non-food (second- and third-generation) biomass feedstocks have come to the forefront as the fourth largest primary energy (Chen et al., 2012) and as the largest source of renewable energy in the world (Hiloidhari et al., 2019). Biomass energy accounted for 14% and up to 90% of renewables globally and in the rural areas of the developing countries, respectively (Sansaniwal et al., 2017). Unlike the first-generation biofuels (food crops), non-food biomass such as crops, agricultural and forest residues, and algae (Yang et al., 2018) does not compromise the limited area of the agricultural ecosystems (Navas-Anguita et al., 2019).

When water hyacinth (*Eichhornia crassipes*) is used as a bioenergy feedstock, it possesses such additional advantages as high growth and propagative performances, high pest and disease resistances, and high litter quality (easy degradation) (Huang et al., 2020). On top of the above superior features is the avoidance of eutrophication of water bodies caused by its invasive nature. Therefore, the utilization of water hyacinth has been explored in different domains. For example, Goel and Kalamdhad (2018) found that the addition of 10% water hyacinth reduced the consumption of fossil fuels required for firing bricks by 7%. Barua and Kalamdhad (2017) increased the maximum biogas output from 143 to 193 mL CH_4/g volatiles solid by pre-treating water hyacinth in a hot air oven. Water hyacinth was also transformed into a high value-added fuel (Zhang et al., 2020), adsorbent (Murambasvina and Mahamadi, 2020), biodiesel products (Alagu et al., 2019), and biochars (Gaurav

---

* Corresponding author.
E-mail address: Liujy@gdut.edu.cn (J. Liu).

https://doi.org/10.1016/j.jclepro.2020.124156

et al., 2020).

There exist only a few studies about the combustion characteristics of water hyacinth. For instance, Huang et al. (2016) emphasized that the addition of water hyacinth improved the co-combustion performance of sludge. The use of K_2CO_3 as a catalyst in the co-combustion of sludge and water hyacinth reduced CO_2, NO_2, SO_2, HCN, and NH_3 emissions (Huang et al., 2018). The previous studies (Alagu et al., 2019; Huang et al., 2016, 2018) about water hyacinth focused on its use as an auxiliary additive in the co-combustions without a comprehensive analysis of its mono-combustion drivers and responses. Before a successful scale-up of the use of water hyacinth in the industrial incineration for the power generation, its comprehensive performance properties in terms of cleaner and efficient production remain to be quantified such as calorific value, reaction mechanism, evolved gases, and ashes. The migration and transformation patterns of the alkali and alkaline earth metallic species (AAEMs) abundantly found in the different biomass parts during the combustion also affect the life cycle of the industrial boilers. This study focused on filling these knowledge gaps in related literature.

Hence, the objectives of this experimental study were to characterize the mono-combustion performances of the two biomass parts of water hyacinth and their reaction mechanisms and evolved gases and to evaluate ash-related issues by using X-ray fluorescence spectrometer (XRF) analysis. The quantification of the above-mentioned characteristics can provide the basis for the scale-up and optimization of their boiler parameters.

2. Material and methods

2.1. Sample preparation and TG-FTIR-MS experiments

Water hyacinth was sampled from a paddy field in Wenzhou in southeast China. The specimens were partitioned into roots (WHR) and stems and leaves (WHSL), cleaned, dried, milled into the particles, and sieved into a diameter of less than 75 μm. Their ultimate and proximate analysis results are showed in Table S1 according to our previous study (Huang et al., 2020). The ash components were measured using an XRF spectrometer (Axios-Minerals, PANalytical, USA).

Detailed information for the TG, TG-FTIR, and TG-MS analyses of the samples can be obtained in the supplementary data section (S1).

2.2. Two-dimensional correlation spectroscopy (2D-COS) analysis

In this study, two-dimensional correlation spectroscopy (2D-COS) analysis was used to detect the subtle and sequential temperature dependency of the functional groups so as to improve the spectral resolution, and thus, to distinguish the overlapping peaks. 2D-COS analysis was performed following the method by Noda and Ozaki (Noda et al., 2000). 20 TG-FTIR spectra data from 180 to 560 °C at an increment of 20 °C were selected for 2D-COS analysis based on which the (a)synchronous 2D-correlation spectra maps were generated using 2D-shige software version 1.3 (Shigeaki Morita, Kwansei-Gakuin University, Japan).

2.3. Combustion performance indices

The following four combustion performance indices were adopted: flammability (C), comprehensive combustion index (CCI), ignition index (D_i), and burnout index (D_b) and were estimated as follows:

$$C = \frac{(-R_p)}{T_i^2} \tag{1}$$

$$CCI = \frac{(-R_p) \times (-R_v)}{T_i^2 \times T_b} \tag{2}$$

$$D_i = \frac{(-R_p)}{t_i \times t_p} \tag{3}$$

$$D_b = \frac{(-R_p)}{\Delta t_{1/2} \times t_p \times t_b} \tag{4}$$

where R_p and R_v are maximum and average weight loss rate, respectively; T_i and T_b are ignition and burnout temperatures, respectively; t_i is ignition time; t_b is burnout temperature; t_p is maximum peak time during which the reaction proceeds at its maximum rate; and $\Delta t_{1/2}$ is half-peak width time range 1/2 (when the weight loss rate reaches 1/2 of the maximum weight loss rate).

2.4. Kinetic analysis

Detailed information for the integral methods of the biomass decomposition could be obtained in the supplementary data section (S1). The iso-conversional methods are used to estimate the activation energy (E_a) without prior-knowledge about the reaction mechanisms involved in the thermochemical conversions of biomass. In this study, the Kissinger-Akahira-Sunose (KAS), Flynn-Wall-Ozawa (FWO), Tang, and Starink methods were applied to estimate E_a. Based on Eq. (S4), the FWO, KAS, Starink (Mishra et al., 2020), and Tang (Jiang et al., 2018) methods can be expressed as follows:

$$\text{FWO}: \log\beta = \log\left(\frac{AE_a}{Rg(\alpha)}\right) - 2.315 - 0.4567\frac{E_a}{RT} \tag{5}$$

$$\text{KAS}: \ln\left(\frac{\beta}{T^2}\right) = \ln\left(\frac{AE_a}{Rg(\alpha)}\right) - \frac{E_a}{RT} \tag{6}$$

$$\text{Tang}: \ln\left(\frac{\beta}{T^{1.894661}}\right) = \ln\left[\frac{AE_a}{Rg(\alpha)}\right] + 3.635041 - 1.894661\ln E_a - 1.001450\frac{E_a}{RT} \tag{7}$$

$$\text{Sarink}: \ln\left(\frac{\beta}{T^{1.92}}\right) = C_s - 1.0008\frac{E_a}{RT} \tag{8}$$

The plots of logβ, ln (β/T^2), ln ($\beta/T^{1.894661}$), and ln ($\beta/T^{1.92}$) versus $1/T$ were obtained whose slopes were used to estimate E_a. In this study, Avrami's theory was extended to determine the reaction order (n) during the non-isothermal combustion process. The variation of the conversion degree with temperature and heating rate can be expressed as follows (Liu et al., 2019):

$$\alpha(T) = 1 - \exp\left(-\frac{K(T)}{\beta^n}\right) \tag{9}$$

Substituting the Arrhenius equation ($K(T) = A\exp\left(-\frac{E_a}{RT}\right)$) into Eq. (9) and taking the double logarithm of both sides yield Eq. (10) below:

$$\ln[-\ln(1-\alpha(T))] = \ln A - \frac{E_a}{RT} - n \ln \beta \tag{10}$$

where the reaction order (n) can be calculated from the slope of the best-fit line of the plot of ln [-ln (1-$\alpha(T)$)] versus lnβ.

The pre-exponential factor (A) was determined according to Eq. (11) below (Maia and de Morais, 2016):

$$A = \left[\beta \cdot E_a \cdot \exp\left(\frac{E_a}{RT_{\max}}\right)\right] \Big/ \left(RT_{\max}{}^2\right) \tag{11}$$

where $T_{\max}$ is maximum peak temperature where the reaction proceeds at its maximum rate, K. The reactivity parameter (R_M) was used to estimate the mean reactivity of the samples as follows (Ghetti et al., 1996):

$$R_M = \frac{R_1}{T_{P1}} + \frac{R_2}{T_{P2}} + \ldots\ldots + \frac{R_n}{T_{Pn}} \tag{12}$$

where R and T_p are the height of the DTG peak and its corresponding temperature, respectively.

In this study, the Coats-Redfern (CR) method was carried out to determine the reaction mechanisms. Assuming 2RT/$E_a \approx 0$, the CR method can be described thus (Zhang et al., 2018):

$$\ln\left(\frac{g(\alpha)}{T^2}\right) = \ln\left(\frac{AR}{\beta E_a}\right) - \frac{E_a}{RT} \tag{13}$$

E_a was estimated from the slope of the best-fit line of the plots of ln ($g(\alpha)/T^2$) versus 1/T. Table S2 shows the common reaction mechanism models (Hu et al., 2019) during a solid-state process. In this study, we chose the model with the highest coefficient of determination (R^2) as the best fit model to describe the reaction mechanism of the thermal degradation of the samples.

3. Results and discussion

3.1. Dynamic thermogravimetric responses

With the increased heating rate, the DTG curves shifted to the higher temperature zone for both WHR and WHSL (Fig. 1a and b) since the high heating rate exacerbated the thermal hysteresis effect of the reaction. The similar DTG responses of the WHR and WHSL combustions to the three heating rates were indicative of the ineffective role of the heating rates. Thus, the curves at 10 °C/min were henceforth chosen to analyze the detailed characteristics of the WHR and WHSL combustions.

The combustion behaviors of WHR and WHSL were characterized by the four degradation stages according to their DTG curves (Fig. 1c and d) (Table S3). As for WHR, the first stage was the evaporation of water between 30 and 159.6 °C, with a maximum mass loss rate of 0.48%/min at 63.7 °C corresponding to the first peak. The second stage corresponded to the combustion of volatiles in the range of 159.6–359.3 °C, with a maximum mass loss rate of 9.99%/min at 317.7 °C. The release of volatiles occurred mainly from the decompositions of (hemi)celluloses and partial lignin (Paniagua Bermejo et al., 2020). The mass loss of the third stage (19.74%) was attributed mainly to the combustion of fixed carbon, with a peak decomposition rate of 2.94%/min at 382.9 °C. When the most volatiles of WHR were released in the second stage, oxygen diffused gradually to the surface of fixed carbon, thus accelerating its combustion. At above 550 °C, the decomposition of minerals in WHR dominated with a little mass loss, and eventually, the combustion reaction of WHR was completed. Wang et al. (2019) reported that the mass loss of rice straw was due to the degradation of (hemi)celluloses in the first stage (189–340 °C) and the decomposition of lignin and the combustion of char in the second stage (340–461 °C).

Unlike WHR with only three peaks, the WHSL combustion had the following four distinct and sequential peaks: (1) the peak of evaporation (0.55%/min at 68.0 °C); the combustion peaks of (2) volatiles (7.45%/min at 290.6 °C) and (3) fixed carbon (5.06%/min at 462.6 °C); and (4) the decomposition peak of minerals (0.65%/min at 847.3 °C). In the second stage, the maximum mass loss was lower for WHSL (7.45%/min) than WHR (9.99%/min), while the mass loss was higher for WHR (58.40%) than WHSL (58.00%). In other words, the WHR combustion performed better in this stage owing to its higher volatiles content than WHSL.

In the third stage, WHSL had a higher maximum mass loss rate and a narrower temperature range than did WHR. At below 500 °C, the decomposition reaction of WHSL appeared completed, with a significant mass loss of 7.97% in the range of 700–1000 °C. This possibly related to the secondary decomposition of residues such as chars and the residue ignition. The significant difference in the (D)TG curves between WHR and WHSL pointed to their different thermal degradation paths. The mass loss peak of WHSL was clearly observed in the high temperature stage. This suggested that WHSL would require a higher temperature (about 900 °C) for its complete reaction in an industrial boiler, whereas the incineration of WHR would realize its complete decomposition at a lower temperature (about 550 °C). In other words, the energy consumption of WHR may be less than that of WHSL. These findings indicated that boilers in industrial applications require different operational parameters to make a more efficient use of the WHR and WHSL feedstocks.

3.2. (D)DSC analyses

The DSC and derivative of DSC (DDSC) curves under the three different heating rates are illustrated in Fig. 2, while the characteristics of the DSC curves are provided in Table S4.

The DSC curve of the WHR combustion showed the two distinct exothermic peaks, as was with that of the WHSL combustion, but was different from its DTG curve with the three distinct mass loss peaks. This was because the combustion reactions of the water evaporation and the light volatiles overlapped, thus rendering the heat flow peak of the water evaporation stage quite subtle. The first and second peak regions were due to the release of volatiles and the combustion of fixed carbon, respectively.

The DSC curve of WHR at 10 °C/min showed that the peak temperatures for the release of volatiles and the fixed carbon combustion were 331.0 and 383.6 °C, respectively, and were higher than its DTG peak temperatures (317.7 and 382.9 °C, respectively). This was attributed to the hysteresis effect between the outer and inner particles to hinder the release of heat. The same also applied to the WHSL combustion.

The heat releases of the first and second peaks of WHR accounted for 37.1–41.4% and 32.2–34.1% of the total heat releases, respectively. The heat releases of the first and second peaks of WHSL explained 56.0–56.4% and 28.1–34.7% of the total heat releases, respectively. With the highest heating rate, the higher total heat release from the WHR (2140.6–4226.7 J/g) than WHSL (1255.6–3110.6 J/g) combustion pointed to the promoted exothermic behavior, the increased energy release, and the better WHR than WHSL combustion. This also suggested that more heat would be generated when WHR is incinerated in the boiler, and thus, WHR is more conducive to the energy recovery of power plants. Their heat releases were lower than those from miscanthus, poplar, and rice husk in the range of 6000–9000 J/g (Kok and Özgür, 2013).

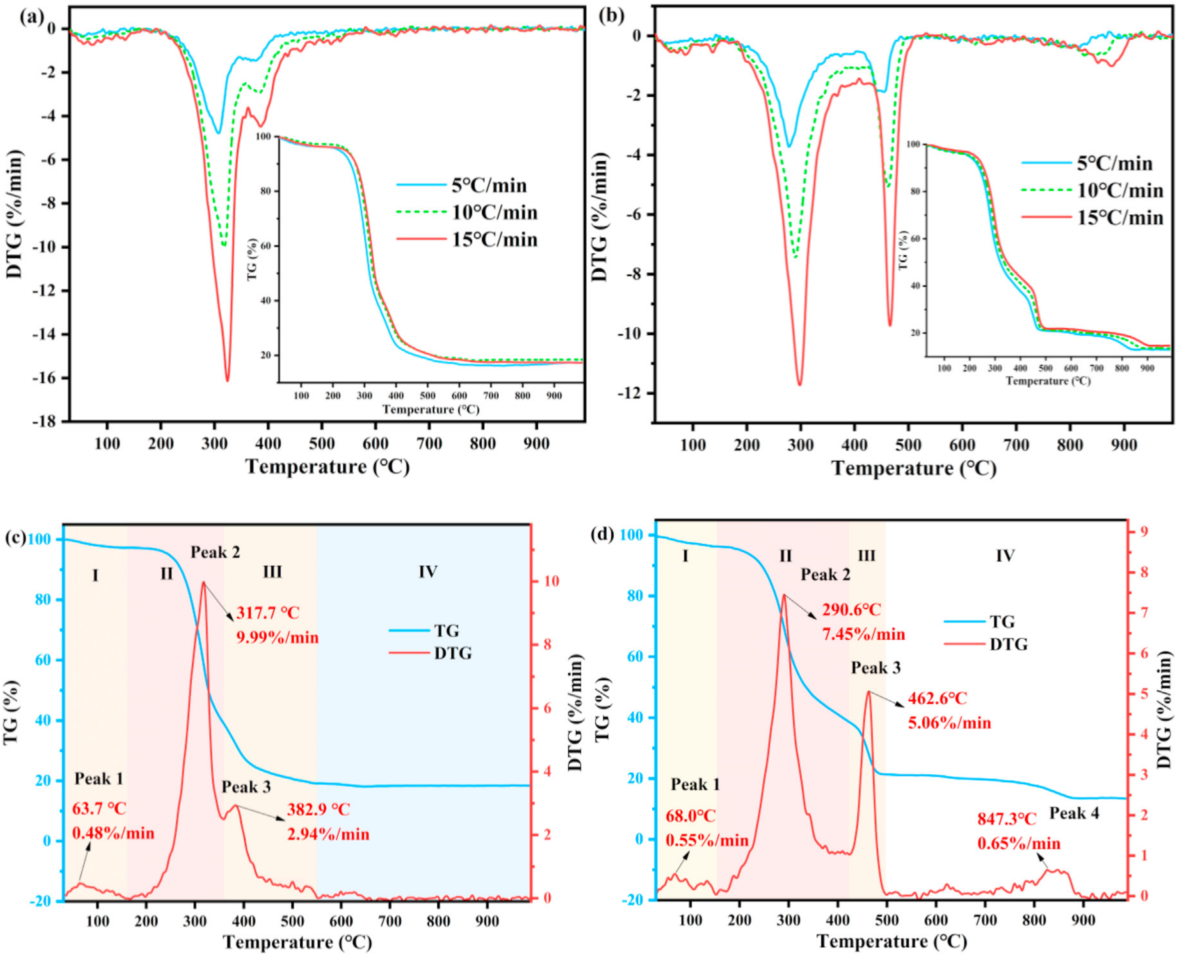

Fig. 1. (D)TG curves of (a) WHR and (b) WHSL combustions under three heating rates; and (D)TG curves of (c) WHR and (d) WHSL combustions at 10 °C/min.

3.3. Performance responses of combustions to increased heating rate

All the combustion performance parameters rose with the elevated heating rates regardless of the biomass part (Table 1). The high flammability index (C) showed a better stability of the solid fuel combustion after the ignition. WHR had a higher C value than did WHSL. Thus, WHR exhibited a more stable combustion, with the conduciveness of the high heating rate to its thermal decomposition.

The high comprehensive combustion index (CCI) reflects a more intense burning and a quicker oxidative decomposition rate. The CCI value was higher for WHR than WHSL. This pointed to a better combustion performance of WHR than WHSL. This may be attributed to the higher burnout temperature of WHSL than WHR. At 10 °C/min, the CCI value of WHR (21.7) was higher than that of camellia seed shell (8.1) (Chen et al., 2017) but lower than that of bamboo branches (24.6) (Hu et al., 2019). WHR had better ignition and burnout performances than did WHSL according to its higher ignition (D_i) and burnout (D_b) indices since WHR had higher volatiles and low ash contents (Thirugnanasambandam et al., 2011). Also, the higher R_p value of WHR than WHSL indicated that the combustion reaction of WHR at the peak temperature was more intense and its reaction activity was higher which in turn significantly shortened the reaction time. In other words, the combustion performance was better for WHR than WHSL, as was consistent with Section 3.1.

3.4. Conversion degree-dependent kinetics and reactivity

Knowledge of the parameters of activation energy (E_a) (the energy barrier of the chemical reaction) and pre-exponential factor (A) (the frequency of collisions between the activated molecules) allows for the predictions of great practical value in solving the scale-up, optimization, and design problems. The iso-conversional plots for E_a are illustrated in Fig. 3, while the estimated kinetic parameters are presented in Table 2 and Fig. S1. The A estimates were derived from the experimental data when $\beta = 10$ °C/min. The R^2 values for the FWO, KAS, Tang, and Starink methods were all higher than 0.9 (Table 2). The R^2 values were higher for the FWO than KAS, Tang, and Starink methods for both WHR and WHSL.

The E_a estimates by the four iso-conversional methods ranged from 137.8 to 190.2 kJ/mol and 85.3–320.8 kJ/mol for WHR and WHSL, respectively. The E_a value of WHR reached its minimum when $\alpha = 0.1$ and its maximum when $\alpha = 0.6$. Its E_a value gradually declined when $\alpha > 0.6$. The α range of 0.1–0.6 belonged to the main degradation stage of hemicellulose, while the α between 0.6 and 0.9 represented the main degradation stage of cellulose.

The trends of E_a for WHSL and WHR were similar in the α range of 0.1–0.5. The E_a value for WHSL plunged when $\alpha > 0.5$ and reached its minimum when $\alpha = 0.7$. The main degradation stages of hemicellulose and cellulose were related to the α ranges of 0.1–0.5 and 0.5–0.7, respectively. When $\alpha > 0.7$, its E_a rose and reached its maximum when $\alpha = 0.9$. This irregular E_a trend was usually attributed to the parallel, competitive, and complex reactions that

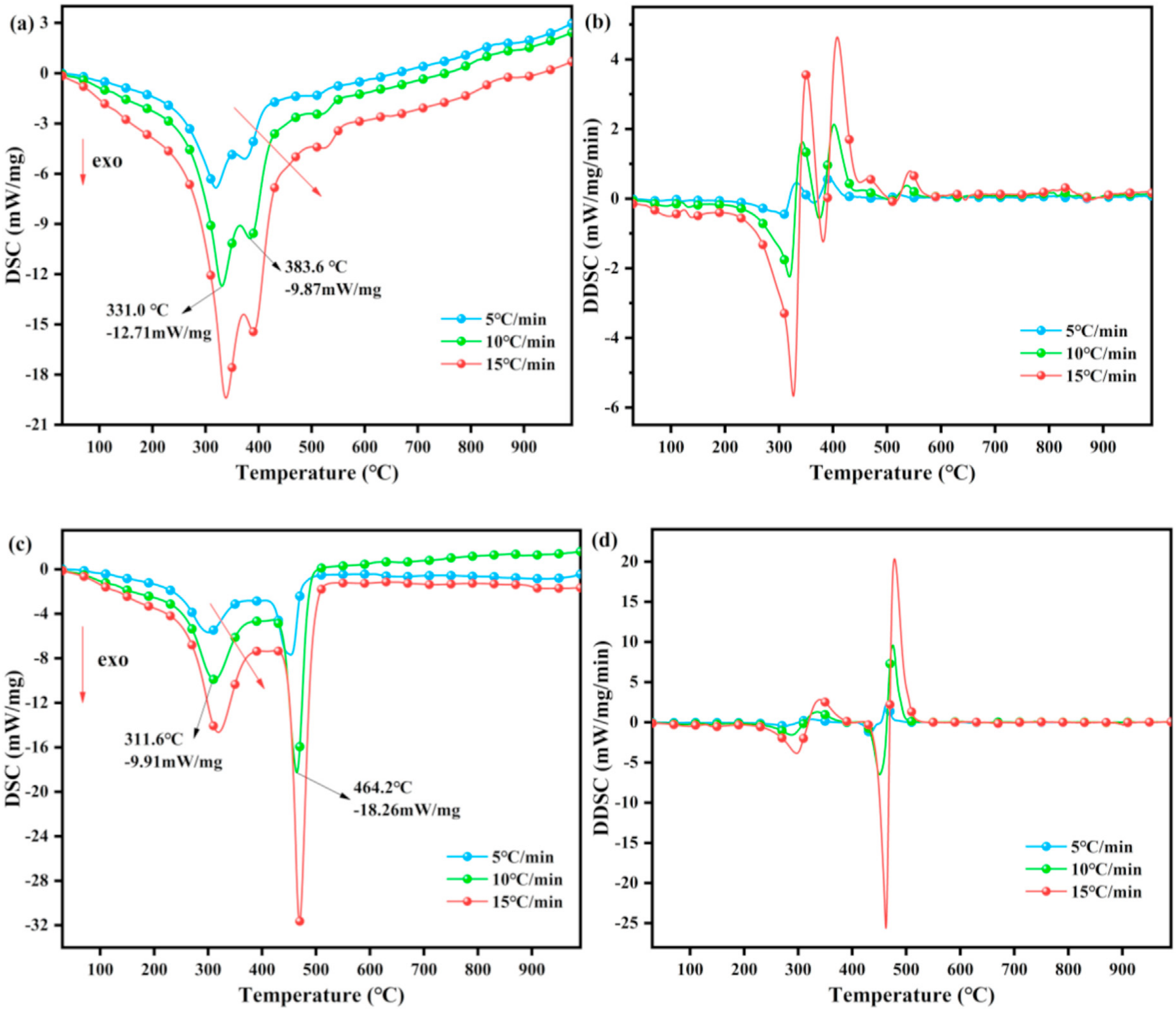

Fig. 2. DSC curves of (a) WHR and (c) WHSL and DDSC curves of (b) WHR and (d) WHSL.

Table 1
Combustion performance responses of WHR and WHSL to an increased heating rate.

Biomass	WHR			WHSL		
β (°C/min)	5	10	15	5	10	15
C ($10^{-5}\cdot\%\cdot\mathrm{min}^{-1}\cdot{}^{\circ}\mathrm{C}^{-2}$)	6.73	13.02	20.10	5.38	11.21	17.17
CCI ($10^{-8}\cdot\%^{2}\ \mathrm{min}^{-2}\ {}^{\circ}\mathrm{C}^{-3}$)	5.83	21.74	50.63	3.01	12.13	28.02
D_i ($10^{-3}\cdot\%\cdot\mathrm{min}^{-3}$)	1.73	13.17	44.09	1.46	11.63	37.41
D_b ($10^{-4}\cdot\%\cdot\mathrm{min}^{-4}$)	0.86	13.98	75.08	0.33	6.31	32.55
$-R_P$ (%/min)	4.78	9.99	16.14	3.37	7.45	11.73
$-Rv$ (%/min)	0.43	0.87	1.37	0.45	0.92	1.42
Temperature (°C)						
T_i	266.7	276.9	283.4	250.2	257.8	261.4
T_b	493.5	518.6	542.0	808.6	849.3	872.0
T_p	307.7	317.7	323.8	278.1	290.6	298.2
Time (min)						
t_i	48.70	25.63	17.94	45.40	23.80	16.65
t_b	94.44	49.96	34.99	157.38	83.05	57.06
t_p	56.92	29.58	20.40	50.97	26.93	18.83
$\Delta t_{1/2}$	10.33	4.83	3.01	12.62	5.28	3.35

occurred in its combustion.

The lower average E_a of WHR than WHSL regardless of the estimation method meant the lower energy barrier of the chemical reaction for WHR than WHSL. Their average E_a values were lower than that of rice (222.3 kJ/mol) (Ming et al., 2020). According to the FWO-method, the higher average A value of WHSL (1.2×10^{27} s^{-1}) than WHR (1.0×10^{14} s^{-1}) verified that the WHSL combustion needed more energy and was proportional to the E_a value of the reaction.

At the same heating rate, WHR had a higher R_M value than did WHSL (Table S5) indicating that the WHR combustion had higher reactivity, that is, easier reactions to carry out. This was because WHR had lower average activation energy than did WHSL. Also, the high heating rate had a higher R_M value which implied the enhanced reactivity. Reaction order (n) of the combustions was estimated according to Avrami's theory (Table S6). The higher average n value of WHSL (5.73) than WHR (4.33) in the range of 275–475 °C suggested a more complicated WHSL combustion. The conversion degree dependency of the n values emphasized the multiple steps involved in the WHR and WHSL combustions.

3.5. *Reaction mechanisms*

In this study, the volatiles (stage II) and fixed carbon (stage III) combustion stages were focused on for their in-depth reaction mechanisms as the representation of the WHR and WHSL combustions (their detailed temperature zones are shown in Table S7). The results of the CR-estimated kinetic parameters based on the 17 common kinetic models are presented in Table S8. The reaction mechanisms of the volatiles and fixed carbon combustion stages

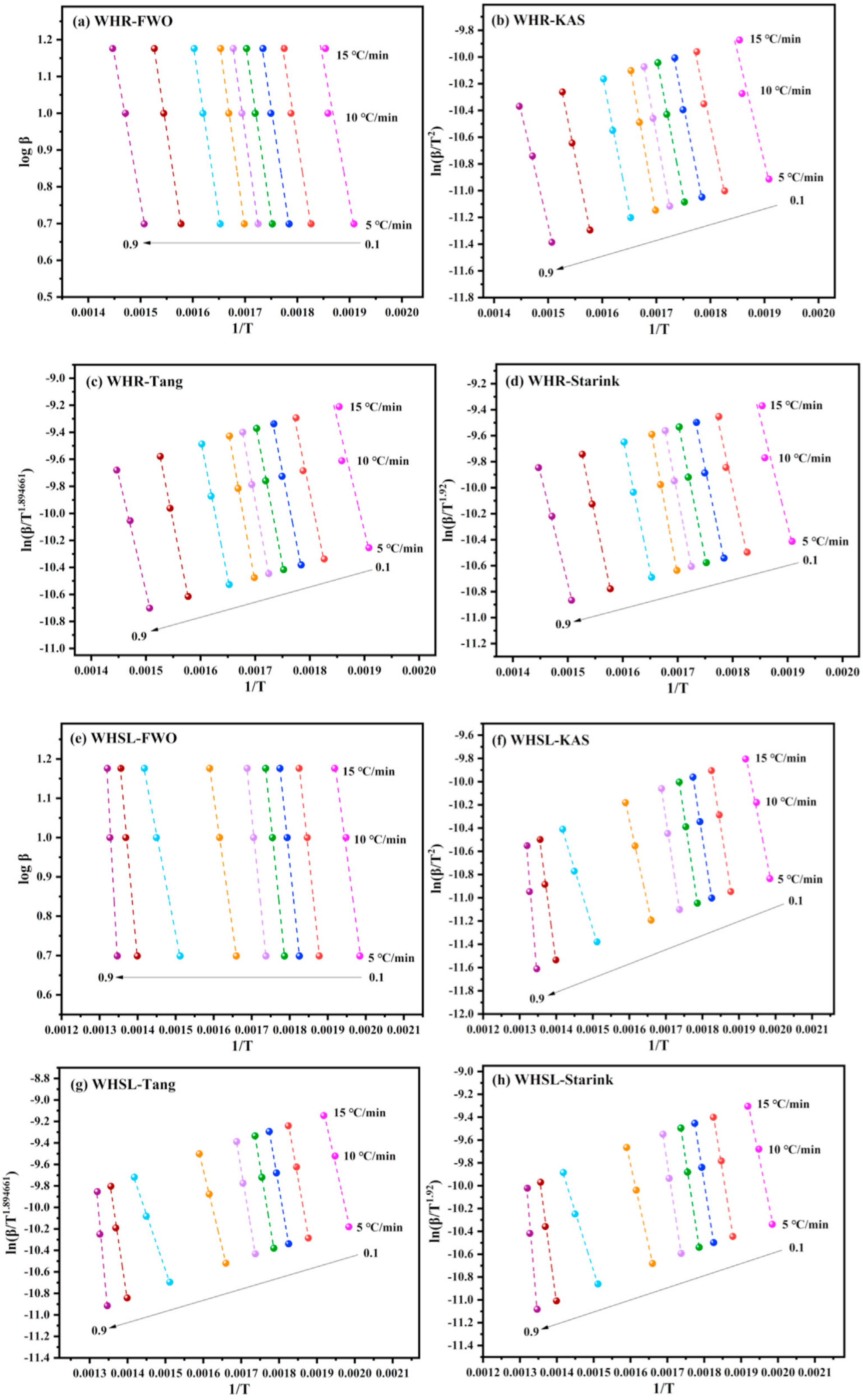

Fig. 3. Iso-conversional plots for activation energy estimation of the WHR and WHSL combustions by the four methods.

were best described by the F1 and F3 models for WHR and by the F3 and F1.5 models for WHSL, respectively (Table 3). Fn as the reaction order model hinges on the fact that the decomposition of particles follows a random nucleation where growth does not advance beyond the individual crystallite nucleated (Fernandez-Lopez et al., 2016). The reaction order of the Fn model differed between the WHR and WHSL combustions. It followed that the reaction mechanisms and the reaction complexity were different in their

Table 2
Conversion degree-dependent kinetic parameters of the mono-combustions.

Sample	α	FWO			KAS			Tang			Starink		
		E_a (kJ/mol)	R^2 (%)	A (s^{-1})	E_a (kJ/mol)	R^2 (%)	A (s^{-1})	E_a (kJ/mol)	R^2 (%)	A (s^{-1})	E_a (kJ/mol)	R^2 (%)	A (s^{-1})
WHR	0.1	139.4	91.63	1.7×10^{10}	137.8	90.63	1.2×10^{10}	138.0	90.69	1.3×10^{10}	138.0	90.67	1.3×10^{10}
	0.2	162.5	98.36	2.2×10^{12}	161.7	98.18	1.8×10^{12}	161.9	98.19	1.9×10^{12}	161.9	98.18	1.9×10^{12}
	0.3	170.4	99.45	1.1×10^{13}	169.7	99.39	9.9×10^{12}	170.0	99.40	1.0×10^{13}	170.0	99.40	1.0×10^{13}
	0.4	175.1	99.84	3.0×10^{13}	174.5	99.82	2.7×10^{13}	174.7	99.82	2.8×10^{13}	174.7	99.82	2.8×10^{13}
	0.5	182.3	99.94	1.4×10^{14}	181.9	99.93	1.3×10^{14}	182.1	99.93	1.3×10^{14}	182.1	99.93	1.3×10^{14}
	0.6	190.1	99.93	6.9×10^{14}	190.0	99.92	6.8×10^{14}	190.2	99.92	7.1×10^{14}	190.2	99.92	7.1×10^{14}
	0.7	172.4	99.87	1.7×10^{13}	171.1	99.86	1.3×10^{13}	171.3	99.86	1.4×10^{13}	171.3	99.86	1.4×10^{13}
	0.8	169.6	99.96	9.5×10^{12}	167.6	99.95	6.3×10^{12}	167.9	99.95	6.8×10^{12}	167.9	99.95	6.7×10^{12}
	0.9	145.0	99.82	5.5×10^{10}	141.3	99.78	2.5×10^{10}	141.7	99.78	2.7×10^{10}	141.6	99.78	2.7×10^{10}
	Mean	167.4		1.0×10^{14}	166.2		9.6×10^{13}	166.4		1.0×10^{14}	166.4		1.0×10^{14}
WHSL	0.1	131.8	99.12	1.4×10^{10}	130.1	99.00	9.4×10^{9}	130.4	99.00	9.9×10^{9}	130.4	99.00	9.9×10^{9}
	0.2	165.4	99.80	2.2×10^{13}	165.0	99.77	2.0×10^{13}	165.2	99.77	2.1×10^{13}	165.2	99.77	2.1×10^{13}
	0.3	169.9	100	5.9×10^{13}	169.4	100	5.3×10^{13}	169.6	100	5.6×10^{13}	169.6	100	5.6×10^{13}
	0.4	174.8	99.99	1.7×10^{14}	174.4	99.99	1.6×10^{14}	174.6	99.99	1.7×10^{14}	174.6	99.99	1.7×10^{14}
	0.5	175.1	99.88	1.9×10^{14}	174.5	99.87	1.6×10^{14}	174.7	99.87	1.7×10^{14}	174.7	99.87	1.7×10^{14}
	0.6	123.9	100	2.3×10^{9}	120.0	100	1.0×10^{9}	120.4	100	1.1×10^{9}	120.3	100	1.1×10^{9}
	0.7	91.9	99.87	1.9×10^{6}	85.3	99.84	4.3×10^{5}	85.8	99.85	4.8×10^{5}	85.7	99.85	4.7×10^{5}
	0.8	198.0	99.37	2.8×10^{16}	196.1	99.29	1.8×10^{16}	196.5	99.29	2.0×10^{16}	196.5	99.29	2.0×10^{16}
	0.9	320.8	98.42	1.1×10^{28}	319.9	98.20	8.8×10^{27}	320.1	98.21	9.2×10^{27}	320.1	98.21	9.3×10^{27}
	Mean	172.4		1.2×10^{27}	170.5		9.8×10^{26}	170.8		1.0×10^{27}	170.8		1.0×10^{27}

Table 3
Combustion kinetic parameters of WHR and WHSL based on the best-fit models.

Sample	Stage	β (°C/min)	Model	$f(\alpha)$	E_a (kJ/mol)	A (s^{-1})	R^2 (%)	Best-fit regression line
WHR	II	5	F1	1-α	104.83	9.3×10^{6}	99.91	$y = -12609.2x + 9.0854$
		10	F1	1-α	111.06	4.5×10^{7}	99.89	$y = -13357.6x + 9.9048$
		15	F1	1-α	112.39	7.2×10^{7}	99.90	$y = -13518.6x + 9.9654$
		Mean			109.43			
	III	5	F3	$(1-\alpha)^3$	179.33	1.0×10^{12}	95.00	$y = -21570.1x + 20.1738$
		10	F3	$(1-\alpha)^3$	180.82	1.3×10^{12}	95.07	$y = -21748.5x + 19.6602$
		15	F3	$(1-\alpha)^3$	172.64	3.0×10^{11}	95.31	$y = -20764.8x + 17.8798$
		Mean			177.60			
WHSL	II	5	F3	$(1-\alpha)^3$	122.19	1.7×10^{9}	99.45	$y = -14697.5x + 14.1148$
		10	F3	$(1-\alpha)^3$	125.60	4.5×10^{9}	99.42	$y = -15107.1x + 14.4056$
		15	F3	$(1-\alpha)^3$	131.16	1.9×10^{10}	99.28	$y = -15776.0x + 15.3676$
		Mean			126.32			
	III	5	F1.5	$(1-\alpha)^{1.5}$	390.37	1.4×10^{26}	99.84	$y = -46953.9x + 51.9158$
		10	F1.5	$(1-\alpha)^{1.5}$	443.47	6.1×10^{29}	99.91	$y = -53339.7x + 59.4828$
		15	F1.5	$(1-\alpha)^{1.5}$	452.96	2.3×10^{30}	99.74	$y = -54481.1x + 60.4013$
		Mean			428.93			

combustions. Gil et al. (2010) reported that the F1 and D3 models accounted for the volatiles and fixed carbon combustion stages of pine sawdust, respectively.

The average E_a values of the stages II and III of WHR were lower than those of WHSL. It should be also noted that the average E_a values of the fixed carbon combustion were higher than those of the volatiles combustion for both WHR and WHSL. It may relate to the fact that breaking the C—C bonds requires more energy than the C—O bonds since fixed carbon contained more C—C bonds than did volatiles.

However, the CR-estimated E_a values can only represent the average value of a specific reaction stage and cannot reflect the complex change regime of the entire combustion process. Therefore, compared to the iso-conversional methods, the CR method may be associated with the relatively large errors in the estimation of the kinetic parameters. To verify the accuracy of the reaction mechanisms, the experimental versus predicted data were compared using the best-fit models. The good match between the predicted and experimental data (Fig. 4) with the R^2 values of >0.9 supported that the calculated kinetic parameters accurately predicted the combustion processes.

3.6. Evolved gases and their temperature dependency

The Gram-Schmidt orthogonalization was performed to quantitatively analyze the entire infrared spectral range of the data so as to cover all the evolved gases. The evolved gases were concentrated mainly in the range of 185—560 °C for WHR and of 170—550 °C for WHSL (Fig. 5c). The Gram-Schmidt orthogonalization curve of the WHR combustion had only one absorption peak at 329 °C, while the WHSL combustion had two absorption peaks at 303 and 447 °C, as was demonstrated by the 3D-infrared spectrum (Fig. 5a and b). The results of the main functional groups detected and their related gases are shown in Table 4. The absorption band range of 4000—3400 cm^{-1} corresponded to the stretching vibration of O—H that demonstrated the formation of H_2O. The C—H stretching vibration was detected in the range of 3150—2700 cm^{-1}, which showed the appearance of CH_4. The formation of CH_4 was mainly attributed to the cleavage of stable methylene and weak bond methoxy. The ranges of 2400—2220 and 780-600 cm^{-1} belonged to the C═O stretching vibration of CO_2 due to the fracturing or reforming of C═O and C—O—C.

The C—O stretching vibration of 2220—2000 cm^{-1} pointed to CO emission. Xu et al. (2017) stated that the incomplete combustions of

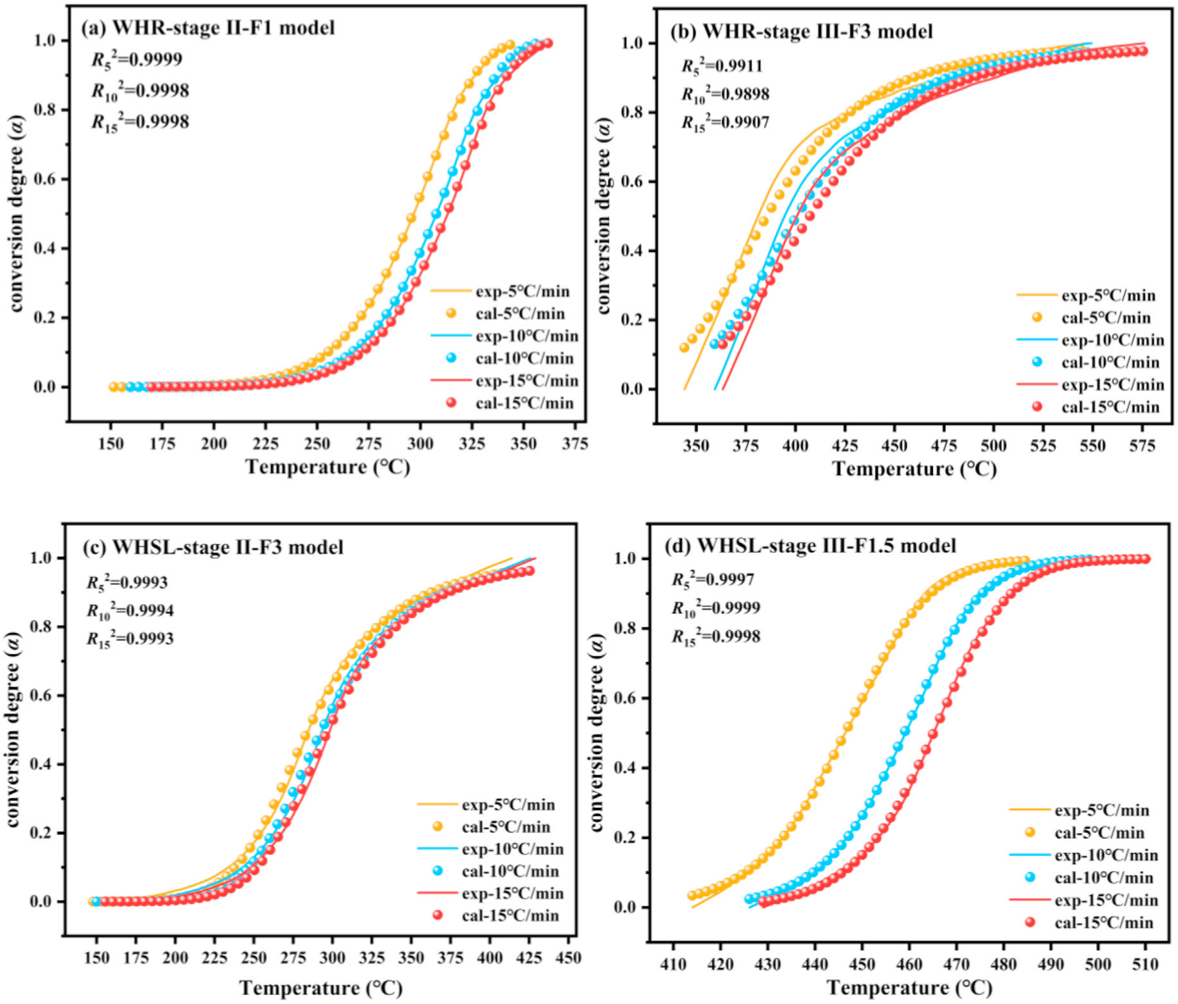

Fig. 4. Experimental (exp) versus predicted (cal) conversion degree (α) based on the best-fit models for each heating rate.

fixed carbon and C_xH_y were the major causes of CO emission. The ranges of 1900–1600 and 1600-1480 cm^{-1} were related to the C═O and C–C benzene skeleton stretching vibrations, respectively, which pointed to the formation of carbonyl-containing compounds (aldehydes, ketones, and acids) and aromatics. The C–O, C–C, and C chain skeleton bending vibrations detected in the range from 1480 to 1000 cm^{-1} corresponded to the existence of alkanes, alcohols, ethers, phenols, and lipids (Zhang et al., 2019). N–H stretching vibration of 966 cm^{-1} was assigned to the formation of NH_3. Quan et al. (2018) found that the main evolved gases of the combustion of corncob hydrogenation residues at the peak temperature of DTG (304.3 °C) were H_2O, CO, CH_4, CO_2, aldehydes, and other organic compounds, with their release intensities closely relating to the temperature.

Since the correlation between the different gas emissions and their temperature dependency cannot be obtained from the TG-FTIR data, 2D-COS analysis was employed instead. In this study, the peaks in the upper-left corner of the (a)synchronous maps (Fig. 6) derived from 2D-COS analysis were counted and analyzed (Table S9). The synchronous maps revealed the dynamic evolution of the different gases in response to the reaction temperature. From the synchronous maps, the eight predominant auto peaks in 683, 1378, 1519, 1750, 2184, 2353, 2937, and 3734 cm^{-1} were observed along the diagonal line for the WHR combustion. The WHSL combustion had the nine predominant auto peaks in 672, 966, 1338, 1509, 1747, 2184, 2361, 2937, and 3734 cm^{-1}.

The highest peak intensities of 2353 and 2361 cm^{-1} for WHR and WHSL, respectively, indicated that CO_2 had the strongest overall sensitivity to the reaction temperature. The signs of the cross-peaks off the diagonal line in the synchronous map were all positive for both WHR and WHSL. The seven positive cross-peaks with a high intensity in 2353/(3734, 2937), 2184/2353, 1750/2353, 1519/2353, 1378/2353, and 966/2353 cm^{-1} were found off the diagonal line in the synchronous map of WHR (Fig. 6a). Based on the Noda's rules, H_2O, CH_4, CO, aldehydes, ketones, acids, aromatics, alkanes, alcohols, phenols, ethers, lipids, and NH_3 simultaneously changed with CO_2. In other words, the spectral changes (increase or decrease) in these gases including CO_2 proceeded in the same directions with the increased temperature which also applied to WHSL (Fig. 6c).

The asynchronous maps of the WHR and WHSL combustions showed some differences. In terms of the Noda's rules and the signs of the peaks showed in Table S9, the sequential changes in the wavenumbers were of the following order: 2353 > 683 > 3734 > 2184 > 1519 > 1378 > 966 > 1750 > 2937 cm^{-1} for WHR and 2361 > 672 > 3734 > 2184 >1509 > 1338 > 2937 > 1747 > 966 cm^{-1} for WHSL. 2353 and 683 cm^{-1} for WHR and 2361 and 672 cm^{-1} for WHSL all represented CO_2 emission, but their sequential orders were different probably due to CO_2 evolved from the different reaction stages. The temperature dependency of the evolved gases

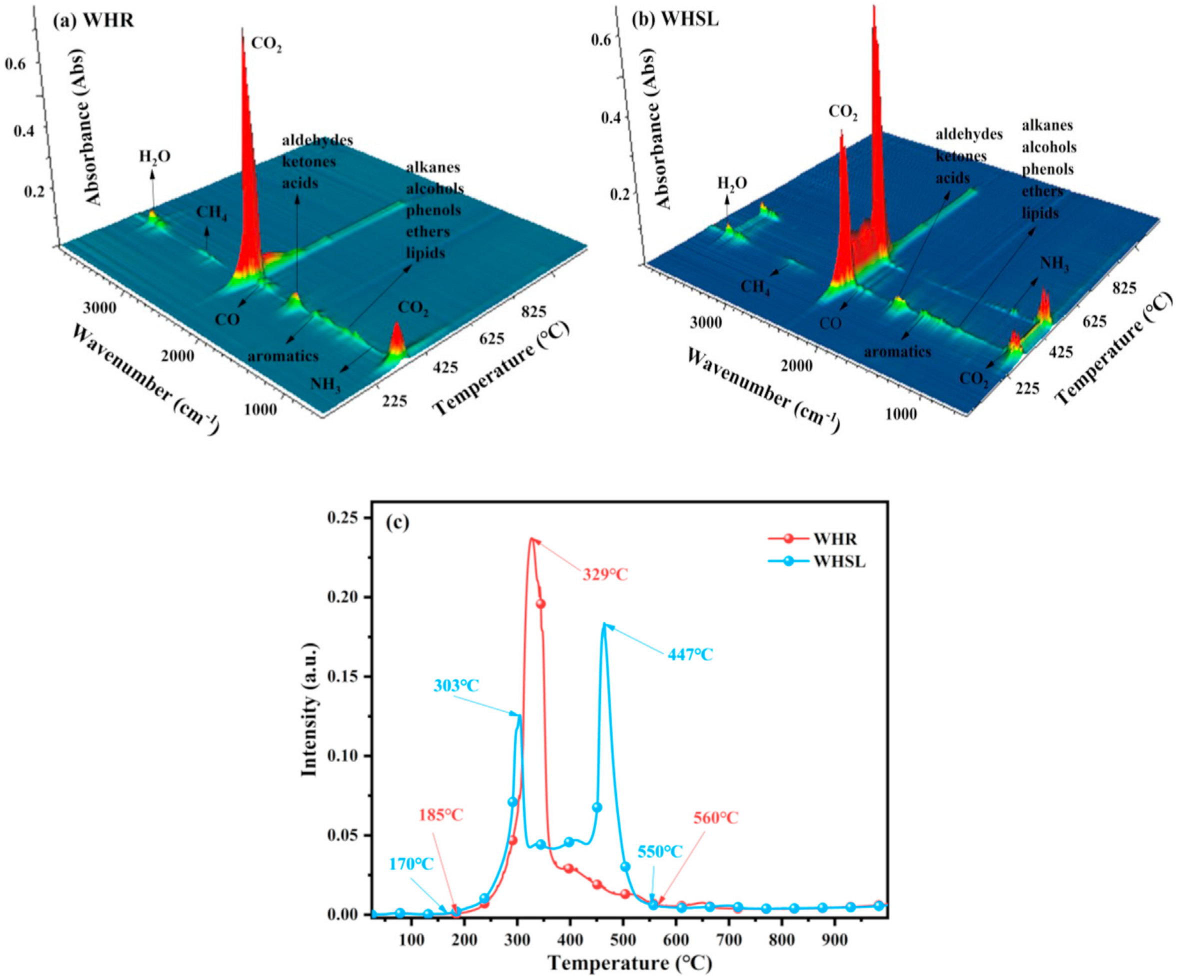

Fig. 5. 3D-infrared spectrum for (a) WHR and (b) WHSL combustions and (c) Gram-Schmidt orthogonalization curve.

Table 4
Main functional groups and their associated gases detected via TG-FTIR analysis.

Wavenumber (cm^{-1})	Functional group	Product	Maximum peak (cm^{-1})	
			WHR	WHSL
4000–3400	O–H stretching vibration	H_2O	3734	3734
3150–2700	C–H asymmetric stretching vibration	CH_4	2937	2937
2400–2220	C=O asymmetric stretching vibration	CO_2	2353	2361
2220–2000	C–O stretching vibration	CO	2184	2184
1900–1600	C=O stretching vibration	aldehydes, ketones, acids	1750	1747
1600–1480	C–C benzene skeleton stretching vibration	aromatics	1519	1509
1480–1000	C–C, C–O and carbon chain skeleton bending vibration	alkanes, alcohols, phenols, ethers, lipids	1378	1338
966	N–H stretching vibration	NH_3	966	966
780–600	C=O asymmetric stretching vibration	CO_2	683	672

was of the following order: $CO_2 > H_2O >$ CO > aromatics > alkanes, alcohols, phenols, ethers, lipids > NH_3 > aldehydes, ketones, acids > CH_4 for WHR, and $CO_2 > H_2O >$ CO > aromatics > alkanes, alcohols, phenols, ethers, lipids > CH_4 > aldehydes, ketones, acids > NH_3 for WHSL. Song et al. (2019) determined the sequential order of the temperature dependency of gases as H_2O/CH_4 > carboxylic acids/ketones > CO_2/ethers, aromatics > CO_2/ethers for the pyrolysis of sugarcane residues. These results pointed to the difference between the biomass pyrolysis and combustion in the temperature-dependent responses of the gases. Based on its fastest response, CO_2 exhibited the strongest dependence on the combustion temperature. This insight can provide an effective reference for the total control on the gas emissions in the future industrial applications of water hyacinth.

3.7. *Emission patterns of small molecular weight gases*

In this study, TG-MS analysis was applied to detect the emission behaviors of small molecular weight gases where the main focus was placed on the ratios of mass to charge (m/z) of 17, 27, 30, 44, 46,

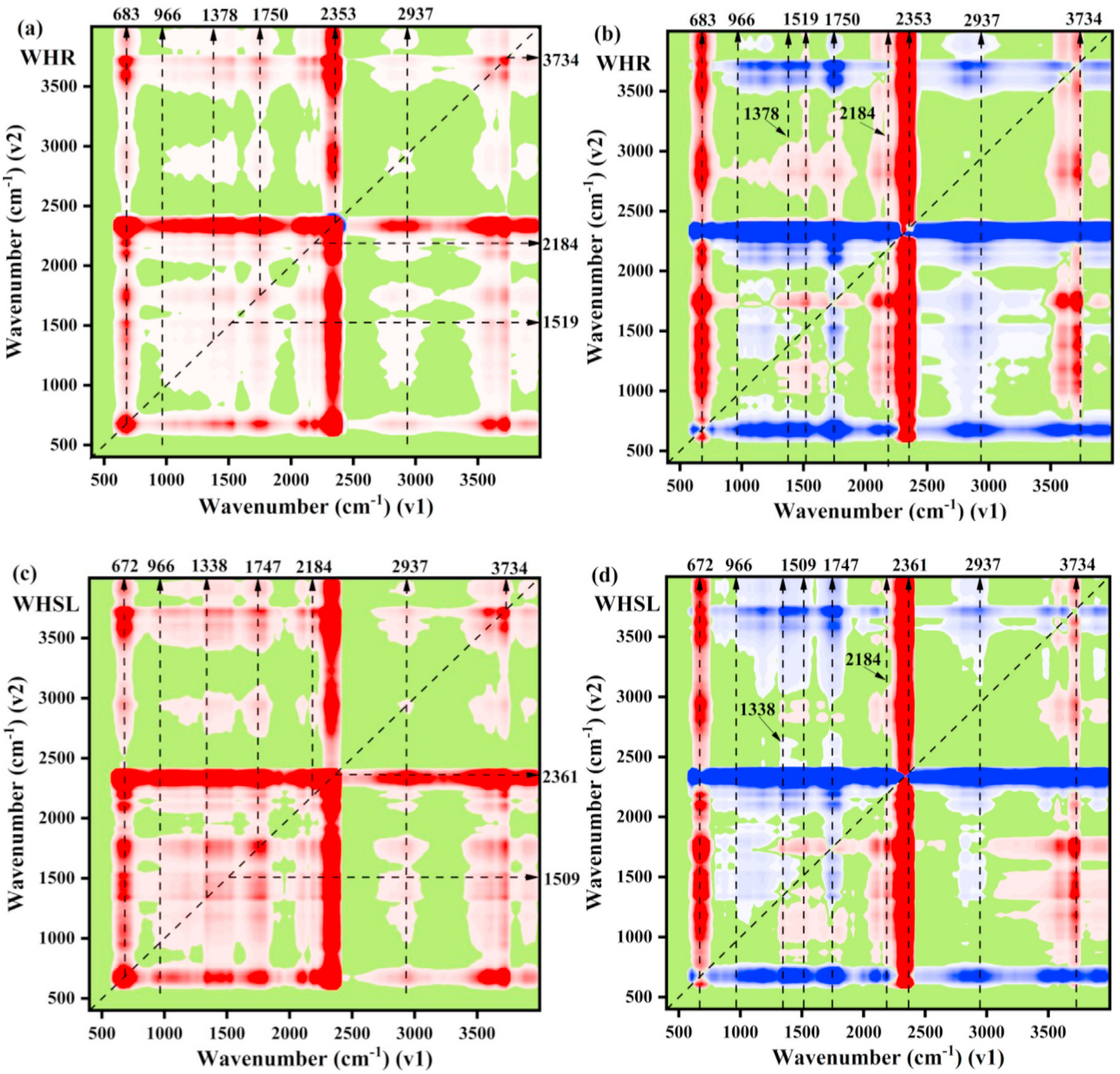

Fig. 6. (a) and (c) Synchronous and (b) and (d) asynchronous maps according to 2D-COS analysis of TG-FTIR results (red/blue/green: positive/negative/zero). (For interpretation of the references to colour in this figure legend, the reader is referred to the Web version of this article.)

60, and 64 that corresponded to NH_3, HCN, NO, CO_2, NO_2, COS, and SO_2, respectively. All the related results are presented in Fig. 7 and Table S10.

As was consistent with Section 3.6, the maximum release intensity of CO_2 belonged to the first and second peaks for WHR and WHSL, respectively (Fig. 7a). Zhang et al. (2019) pointed out that the first and second peaks appeared to relate to the releases of CO_2 from volatiles substances at below 400 °C and from the solid-phase coking polymerization process, respectively. The same evolution trends of the low NH_3 level at below 160 °C existed for both WHR and WHSL, but the different trends occurred in their main reaction zone of 180–540 °C for WHR and 160–530 °C for WHSL (Fig. 7b). NH_3 was previously reported to stem mainly from volatiles-N in the range of 200–400 °C during the volatiles combustion and partly from the char-N combustion at above 400 °C (Zou et al., 2020). Most of NH_3 was released from the volatiles combustion stage of WHR, while due to its high intensity release at this stage, NH_3 release from the fixed carbon combustion stage did not form a peak. At above 530 °C, WHR and WHSL exhibited the same trend that NH_3 rose with the temperature rise due to its secondary release from the residues.

The release patterns of HCN were similar to those of NH_3 for the two samples. Hu et al. (2019) emphasized that the degradation of the intermediate heterocyclic-N compounds at below 350 °C may be the primary driver of HCN emission. The H radical concentration and the interactions between H radicals and N-containing structures on the carbon surface may affect the release pattern of HCN (Zou et al., 2020).

Driven by the oxidation reactions and temperature, HCN and NH_3 were converted to NO_x and acted as its precursors. The main reaction zone of NO for WHR ranged from 200 to 600 °C with three release peaks of the decreasing intensity. The narrower main release interval and the higher maximum release peak intensity of WHSL (180–540 °C) than WHR pointed to the different formation mechanisms of NO. After the third peaks at 521 °C for WHR and at 489 °C for WHSL were reached, the release intensity of NO fell quickly. This was because the NO-char reactions played a key role in the reduction of NO with the following possible reactions (Gao et al., 2016):

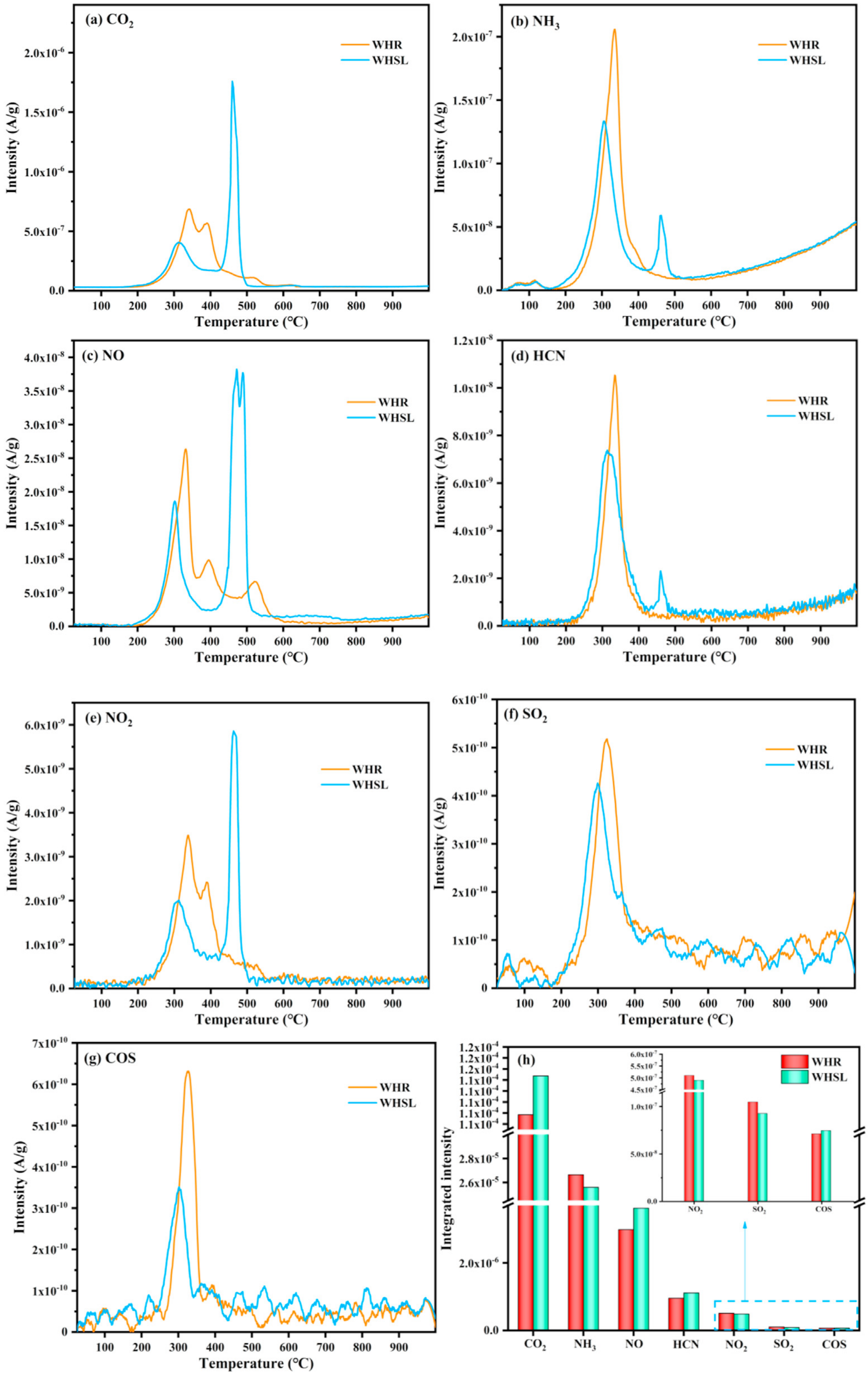

Fig. 7. (a–g) Temperature-dependent emissions and (h) integrated intensities of gases evolved from the WHR and WHSL combustions.

$$2NO + C \rightarrow N_2 + CO_2 \quad (14)$$

$$NO + C \rightarrow \frac{1}{2}N_2 + CO \quad (15)$$

The release responses of NO_2 and CO_2 were similar at the low temperatures. NO_2 emission rose based on the following possible reaction:

$$NO + O_2 = NO_2 + O \quad (16)$$

The N-containing gases were mainly derived from the fuel-N existed as the amino acid and protein and can be divided into volatiles-N and char-N. Fang et al. (2019) stated that most of fuel-N existed as volatiles-N, while only a small quantity of fuel-N existed as char-N as volatiles were released. The fuel-N conversion process during the biomass combustion was divided into three stages. First, the large quantities of NH_3 and HCN were precipitated from the devolatilization stage. Second, during the volatiles combustion stage, volatiles-N was converted to NH_3, HCN, and NO_x and its derivatives in the presence of O_2, NH_3, and HCN. Finally, during the fixed carbon combustion stage, some N-containing compounds previously adsorbed by the chars were oxidized to NO_x, while the rest was reduced to N_2 (Fang et al., 2019).

SO_2 and COS were the typical representatives of S-containing gases in this study. At the evaporation stage, a small quantity of SO_2 was generated with the release of light volatiles decomposed from the unstable side chains of the biomass samples. With the rising temperature, more volatiles were released from the solid-state process, while SO_2 was released in a large quantity from the volatiles combustion stage and peaked at 324 °C for WHR and at 300 °C for WHSL. This indicated that the S residues in the samples were present mainly as the volatiles compounds. The SO_2 concentration dropped sharply and fluctuated in a narrow range at above 530 °C due to the release of inorganic S at the higher temperature. The reduction of SO_2 at the high temperature was driven mainly by the capture of Ca with the following possible reactions (Cheng et al., 2019):

$$CaCO_3 + SO_2 + \frac{1}{2}O_2 \rightarrow CaSO_4 + CO_2 \tag{17}$$

$$CaO + SO_2 \rightarrow CaSO_4 + \frac{1}{2}O_2 \tag{18}$$

The release responses of COS and SO_2 were similar due to the incomplete combustion of S.

Once standardized, the MS data along with the integrated release intensity of the evolved gases enabled the total gas emissions to be obtained (Fig. 7h). CO_2 emission was the highest evolved gas (77.5% for WHR and 78.7% for WHSL) followed by N-containing gases, with S-containing gases as the lowest one (0.13% for WHR and 0.12% for WHSL). This result was consistent with the physicochemical drivers characterized in Table S1. Wang et al. (2019) found the same intensity pattern of gas emissions from the rice husk combustion as our results: $CO_2 > NO > NO_2 > SO_2$. WHSL emitted more CO_2, NO, HCN, and COS than did WHR. These differences stemmed from their different chemical compositions and the different reactions in their combustions. Water hyacinth was a CO_2-neutral feedstock. The emissions of air pollutants such as sulfide and nitride are generally the criteria to decide whether or not a biomass feedstock can be used in the generation of cleaner energy. Both WHR and WHSL resulted in very low levels of sulfide emissions. However, NH_3 emissions from WHR and WHSL accounted for the largest proportion of their polluting gas emissions. In other words, NH_3 emission is a key control factor in the scale-up of the water hyacinth combustion for the real-time industrial applications. Also, staged fuel combustion, flue-gas recirculation, and flue-gas denitrification may be adopted as the best management practices to reduce N-related emissions from the WHR and WHSL combustions.

3.8. *Ash components, evolutions, and deposition issues*

Fig. 8 shows that SiO_2, CaO, MnO, and Al_2O_3 were the main components of the WHR ash, with the clay minerals (SiO_2 and Al_2O_3) accounting for 39.3% by weight. The higher clay mineral contents were reported to increase the ash fusion temperature. The total Na_2O, Cl, and TiO_2 content of the WHR ash was very small (2.3%). Relative to the WHR ash, the WHSL ash were rich in K_2O, CaO, and Cl and low in Fe_2O_3, MnO, and TiO_2.

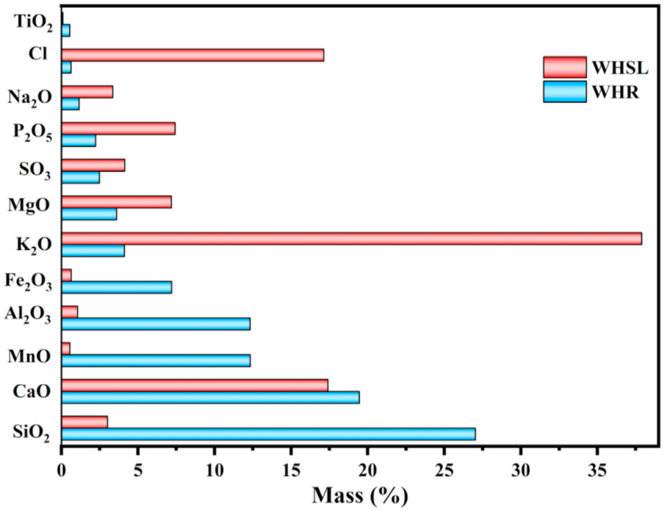

Fig. 8. Ash components of the WHR and WHSL combustions according to XRF analysis.

The higher alkali metal oxide (K_2O and Na_2O) content of the WHSL than WHR ash by about eight times suggested that alkali metals-induced slagging may be more serious for the WHSL combustion. During the combustion, the excess alkaline components were easily evaporated, condensed, and reacted with the silicate melts to form a low melting point eutectic. This was in turn conducive to the formation of the liquid phases which may act as a flue to stimulate the ash-related issues of slagging and fouling (Yao et al., 2020). The Cl content of the WHSL ash (17.1%) was about 27 times that of the WHR ash (0.6%). Cl was present in the biomass fuels as easily evaporated chlorides, a high-temperature transport medium for K and Na. The presence of Cl was previously found to accelerate the high temperature corrosion of the metal surface by KCl (Niu et al., 2016). The higher the Cl content is, the more serious the ash-related problems are.

If a biomass feedstock becomes the input to a boiler, then a relatively accurate prediction of the slagging/fouling trend becomes necessary for a boiler design. For the practical applications, some empirical indices based on the ash composition were developed to predict the slagging and fouling tendencies. The empirical indices estimated for the WHR and WHSL ashes are presented in Table 5. The higher base/acid ratios of the WHSL than WHR ash pointed to the higher fouling tendency of the WHSL ash since it had higher K_2O and Na_2O contents. The lower fouling index (F_u) of WHR (4.7) than WHSL (659.9) ash was attributed to the high SiO_2 and Al_2O_3 contents of the WHR ash. The WHSL ash had an extremely high risk of fouling according to the deposition criteria for F_u. The slagging index (R_S) showed that the WHR ash had a low risk of slagging, whereas the WHSL ash had an extremely high risk of slagging. Based on the sintering tendency (I) index, the WHR ash had no sintering tendency, unlike the WHSL ash. Overall, given all the empirical indices, the slagging and fouling tendencies of the WHSL ash were larger than those of the WHR ash. Guo et al. (2020) reported that leaching pretreatment, in particular, hydrochloric acid leaching, effectively removed AAEMs, and thus, reduced the risk of ash deposition since leaching formed some small structures on the biomass surface which was conducive to gas transportation. Therefore, leaching pretreatment of WHSL may be one of the

Table 5
Empirical indices of the ash deposition-related issues of slagging and fouling for the sample ashes.

Empirical index	Formula (Chen et al., 2020; García et al., 2015; Wang et al., 2017)	WHR	WHSL	Deposition criteria
Base/acid ratio	$R_{B/A} = (Fe_2O_3 + CaO + MgO + K_2O + Na_2O)/(SiO_2 + TiO_2 + Al_2O_3)$	0.89	16.01	<0.5 → low 0.5–1.0 → medium >1.0 → high
Base/acid ratio (contain P_2O_5)	$R_{B/A+P} = (Fe_2O_3 + CaO + MgO + K_2O + Na_2O + P_2O_5)/(SiO_2 + TiO_2 + Al_2O_3)$	0.95	4.12	<0.5 → low 0.5–1.0 → medium >1.0 → high
Fouling index	$F_u = R_{B/A}\ (Na_2O + K_2O)$	4.68	659.91	<0.6 → low 0.6–40 → high >40 → extremely high
Total alkali index	$TA = K_2O + Na_2O$	5.26	41.23	<0.3 → low 0.3–0.4 → medium >0.4 → high
Slagging index	$R_S = R_{B/A}\cdot S$	0.02	5.60	<0.6 → low 0.6–2.0 → medium 2.0–2.6 → high >2.6 → extremely high
Slag viscosity index	$S_R = 100\cdot SiO_2/(SiO_2 + Fe_2O_3 + CaO + MgO)$	47.19	10.66	>78 → low 66.1–78 → medium <66.1 → high
Sintering index	$I = (CaO + MgO)/(K_2O + Na_2O)$	4.38	0.60	>2 no sinter
Fusion temp index	$F = (SiO_2 + K_2O + P_2O_5)/(CaO + MgO)$	1.45	1.97	higher tendency with higher F

S was sulfur content (%) based on ultimate analysis, while the other element/oxide symbols referred to their weight percentages obtained from XRF analysis.

effective ways to reduce the risk of ash deposition.

3.9. Implications for theory and practice

The temperature sensitivity of their CO_2 emissions can be leveraged to dynamically exert a control on the total emissions. The combustion characteristics of the two parts of water hyacinth quantified in this study can provide the basis for the scale-up, optimization, and design of the future incinerators. 550 °C and 900 °C determined for the complete decompositions of WHR and WHSL, respectively, can be used as the optimal constant combustion temperatures for the industrial boilers. The lower activation energy and better combustion performance of WHR pointed to its lower industrial application cost than WHSL and constituted a key consideration in prioritizing the alternative inputs. The gas emissions and their temperature dependency characterized in this study can pave the way for the controls on air pollutants of their boiler combustions. The formation of nitrides and NH_3 appeared as the primary focus of pollution controls that industrial practices need to exert on their combustions. The direct incineration of WHSL was found prone to a high risk of ash deposition, thus signaling the hidden dangers, certain warnings, and preventive and mitigative measures for industrial applications. In the future studies, pilot-scale experiments as well as corrosion experiments still remain to be carried out for the validation of our results. Studies also remain to be conducted about the denitrification of the thermochemical conversions of biomass in order to reduce NO_x emission.

4. Conclusion

The main decomposition stages of the biomass mono-combustions occurred between 159.6 and 549.4 °C for WHR and between 149.9 and 499.0 °C for WHSL, both of which were similar to a typical biomass feedstock (200–500 °C). WHR exhibited a better combustion performance than did WHSL based on its higher total heat release, higher flammability comprehensive combustion indices, easier and different reaction mechanisms, less CO_2, NO, HCN, and COS emissions, and lower risk of ash deposition. Among the evolved gases, CO_2 emission was fastest in its response to the temperature rise from both WHR and WHSL.

Credit author statement

Hongyi Huang: Methodology, Software, Validation, Formal analysis, Investigation, Data curation, Writing - original draft, Writing - review & editing. **Jingyong Liu:** Conceptualization, Methodology, Resources, Writing - review & editing, Project administration, Funding acquisition. **Hui Liu:** Formal analysis, Software, Data curation. **Jinwen Hu:** Methodology, Software. **Fatih Evrendilek:** Data curation, Modeling, Writing - review & editing.

Declaration of competing interest

The authors declare that they have no known competing financial interests or personal relationships that could have appeared to influence the work reported in this paper.

Acknowledgement

This study was supported by the National Natural Science Foundation of China (No. 51978175) and Science and Technology Planning Project of Guangdong Province, China (No. 2018A050506046, 2019SN114, and 2019B020208017).

Appendix A. Supplementary data

Supplementary data to this article can be found online at https://doi.org/10.1016/j.jclepro.2020.124156.

References

Alagu, K., Venu, H., Jayaraman, J., Raju, V.D., Subramani, L., Appavu, P., S, D., 2019. Novel water hyacinth biodiesel as a potential alternative fuel for existing unmodified diesel engine: performance, combustion and emission characteristics. Energy 179, 295–305.

Barua, V.B., Kalamdhad, A.S., 2017. Biochemical methane potential test of untreated and hot air oven pretreated water hyacinth: a comparative study. J. Clean. Prod. 166, 273–284.

Chen, C., Huang, Y., Qin, S., Huang, D., Bu, X., Huang, H., 2020. Slagging tendency estimation of aquatic microalgae and comparison with terrestrial biomass and waste. Energy 194, 116889.

Chen, J., Wang, Y., Lang, X., Ren, X.e., Fan, S., 2017. Comparative evaluation of thermal oxidative decomposition for oil-plant residues via thermogravimetric analysis: thermal conversion characteristics, kinetics, and thermodynamics. Bioresour. Technol. 243, 37–46.

Chen, W.-H., Lu, K.-M., Tsai, C.-M., 2012. An experimental analysis on property and structure variations of agricultural wastes undergoing torrefaction. Appl. Energy 100, 318–325.

Chen, W.H., Lin, B.J., Huang, M.Y., Chang, J.S., 2015. Thermochemical conversion of microalgal biomass into biofuels: a review. Bioresour. Technol. 184, 314–327.

Cheng, S., Zhang, H., Chang, F., Zhang, F., Wang, K., Qin, Y., Huang, T., 2019. Combustion behavior and thermochemical treatment scheme analysis of oil sludges and oil sludge semicokes. Energy 167, 575–587.

Fang, P., Gong, Z., Wang, Z., Meng, F., 2019. Study on combustion and emission characteristics of microalgae and its extraction residue with TG-MS. Renew. Energy 140, 884–894.

Fernandez-Lopez, M., Pedrosa-Castro, G.J., Valverde, J.L., Sanchez-Silva, L., 2016. Kinetic analysis of manure pyrolysis and combustion processes. Waste Manag. 58, 230–240.

Gao, Y., Tahmasebi, A., Dou, J., Yu, J., 2016. Combustion characteristics and air pollutant formation during oxy-fuel co-combustion of microalgae and lignite. Bioresour. Technol. 207, 276–284.

García, R., Pizarro, C., Álvarez, A., Lavín, A.G., Bueno, J.L., 2015. Study of biomass combustion wastes. Fuel 148, 152–159.

Gaurav, G.K., Mehmood, T., Cheng, L., Klemeš, J.J., Shrivastava, D.K., 2020. Water hyacinth as a biomass: a review. J. Clean. Prod. 277, 122214.

Ghetti, P., Ricca, L., Angelini, L., 1996. Thermal analysis of biomass and corresponding pyrolysis products. Fuel 75 (5), 565–573.

Gil, M.V., Casal, D., Pevida, C., Pis, J.J., Rubiera, F., 2010. Thermal behaviour and kinetics of coal/biomass blends during co-combustion. Bioresour. Technol. 101, 5601–5608.

Goel, G., Kalamdhad, A.S., 2018. A practical proposal for utilisation of water hyacinth: recycling in fired bricks. J. Clean. Prod. 190, 261–271.

Guo, Q., Cheng, Z., Chen, G., Yan, B., Hou, L.a., Ronsse, F., 2020. Optimal strategy for clean and efficient biomass combustion based on ash deposition tendency and kinetic analysis. J. Clean. Prod. 271, 122529.

Hiloidhari, M., Baruah, D.C., Kumari, M., Kumari, S., Thakur, I.S., 2019. Prospect and potential of biomass power to mitigate climate change: a case study in India. J. Clean. Prod. 220, 931–944.

Hu, J., Yan, Y., Evrendilek, F., Buyukada, M., Liu, J., 2019. Combustion behaviors of three bamboo residues: gas emission, kinetic, reaction mechanism and optimization patterns. J. Clean. Prod. 235, 549–561.

Huang, H., Liu, J., Liu, H., Evrendilek, F., Buyukada, M., 2020. Pyrolysis of water hyacinth biomass parts: bioenergy, gas emissions, and byproducts using TG-FTIR and Py-GC/MS analyses. Energy Convers. Manag. 207, 112552.

Huang, L., Liu, J., He, Y., Sun, S., Chen, J., Sun, J., Chang, K., Kuo, J., Ning, X., 2016. Thermodynamics and kinetics parameters of co-combustion between sewage sludge and water hyacinth in CO_2/O_2 atmosphere as biomass to solid biofuel. Bioresour. Technol. 218, 631–642.

Huang, L., Xie, C., Liu, J., Zhang, X., Chang, K., Kuo, J., Sun, J., Xie, W., Zheng, L., Sun, S., Buyukada, M., Evrendilek, F., 2018. Influence of catalysts on co-combustion of sewage sludge and water hyacinth blends as determined by TG-MS analysis. Bioresour. Technol. 247, 217–225.

Jiang, L., Zhang, D., Li, M., He, J.-J., Gao, Z.-H., Zhou, Y., Sun, J.-H., 2018. Pyrolytic behavior of waste extruded polystyrene and rigid polyurethane by multi kinetics methods and Py-GC/MS. Fuel 222, 11–20.

Kok, M.V., Özgür, E., 2013. Thermal analysis and kinetics of biomass samples. Fuel Process. Technol. 106, 739–743.

Liu, T., Lang, Q., Xia, Y., Chen, Z., Li, D., Ma, J., Gai, C., Liu, Z., 2019. Combination of hydrothermal carbonization and oxy-fuel combustion process for sewage sludge treatment: combustion characteristics and kinetics analysis. Fuel 242, 265–276.

Maia, A.A.D., de Morais, L.C., 2016. Kinetic parameters of red pepper waste as biomass to solid biofuel. Bioresour. Technol. 204, 157–163.

Ming, X., Xu, F., Jiang, Y., Zong, P., Wang, B., Li, J., Qiao, Y., Tian, Y., 2020. Thermal degradation of food waste by TG-FTIR and Py-GC/MS: pyrolysis behaviors, products, kinetic and thermodynamic analysis. J. Clean. Prod. 244, 118713.

Mishra, A., Kumari, U., Turlapati, V.Y., Siddiqi, H., Meikap, B.C., 2020. Extensive thermogravimetric and thermo-kinetic study of waste motor oil based on iso-conversional methods. Energy Convers. Manag. 221, 113194.

Murambasvina, G., Mahamadi, C., 2020. Effective fluoride adsorption using water hyacinth beads doped with hydrous oxides of aluminium and iron. Ground. Sust. Dev. 10, 100302.

Navas-Anguita, Z., García-Gusano, D., Iribarren, D., 2019. A review of techno-economic data for road transportation fuels. Renew. Sustain. Energy Rev. 112, 11–26.

Niu, Y., Tan, H., Hui, S.e., 2016. Ash-related issues during biomass combustion: alkali-induced slagging, silicate melt-induced slagging (ash fusion), agglomeration, corrosion, ash utilization, and related countermeasures. Prog. Energ. Combust. 52, 1–61.

Noda, I., Dowrey, A.E., Marcott, C., Story, G.M., Ozaki, Y., 2000. Generalized two-dimensional correlation spectroscopy. Appl. Spectrosc. 54, 236A–248A.

Paniagua Bermejo, S., Prado-Guerra, A., García Pérez, A.I., Calvo Prieto, L.F., 2020. Study of quinoa plant residues as a way to produce energy through thermogravimetric analysis and indexes estimation. Renew. Energy 146, 2224–2233.

Quan, C., Ma, Z., Gao, N., He, C., 2018. Pyrolysis and combustion characteristics of corncob hydrolysis residue. J. Anal. Appl. Pyrol. 130, 72–78.

Sansaniwal, S.K., Rosen, M.A., Tyagi, S.K., 2017. Global challenges in the sustainable development of biomass gasification: an overview. Renew. Sustain. Energy Rev. 80, 23–43.

Song, F., Li, T., Zhang, J., Wang, X., Bai, Y., Giesy, J.P., Xing, B., Wu, F., 2019. Novel insights into the kinetics, evolved gases, and mechanisms for biomass (sugar cane residue) pyrolysis. Environ. Sci. Technol. 53 (22), 13495–13505.

Thirugnanasambandam, M., Hasanuzzaman, M., Saidur, R., Ali, M.B., Rajakarunakaran, S., Devaraj, D., Rahim, N.A., 2011. Analysis of electrical motors load factors and energy savings in an Indian cement industry. Energy 36 (7), 4307–4314.

Wang, T., Hou, H., Ye, Y., Rong, H., Li, J., Xue, Y., 2019. Combustion behavior of refuse-derived fuel produced from sewage sludge and rice husk/wood sawdust using thermogravimetric and mass spectrometric analyses. J. Clean. Prod. 222, 1–11.

Wang, Y., Tan, H., Wang, X., Du, W., Mikulci, H., Duic, N., 2017. Study on extracting available salt from straw/woody biomass ashes and predicting its slagging/fouling tendency. J. Clean. Prod. 155, 164–171.

Xu, S., Liu, J., Cao, W., Li, Y., Cao, W., 2017. Experimental study on the minimum ignition temperature and combustion kinetics of coal dust/air mixtures. Powder Technol. 317, 154–161.

Yang, Q., Zhou, H., Zhang, X., Nielsen, C.P., Li, J., Lu, X., Yanga, H., Chen, H., 2018. Hybrid life-cycle assessment for energy consumption and greenhouse gas emissions of a typical biomass gasification power plant in China. J. Clean. Prod. 205, 661–671.

Yao, X., Zheng, Y., Zhou, H., Xu, K., Xu, Q., Li, L., 2020. Effects of biomass blending, ashing temperature and potassium addition on ash sintering behaviour during co-firing of pine sawdust with a Chinese anthracite. Renew. Energy 147, 2309–2320.

Zhang, C., Ma, X., Chen, X., Tian, Y., Zhou, Y., Lu, X., Huang, T., 2020. Conversion of water hyacinth to value-added fuel via hydrothermal carbonization. Energy 197, 117193.

Zhang, Y., Kang, L., Li, H., Huang, X., Liu, X., Guo, L., Huang, L., 2019. Characterization of moxa floss combustion by TG/DSC, TG-FTIR and IR. Bioresour. Technol. 288, 121516.

Zhang, Z., Wang, C., Huang, G., Liu, H., Yang, S., Zhang, A., 2018. Thermal degradation behaviors and reaction mechanism of carbon fibre-epoxy composite from hydrogen tank by TG-FTIR. J. Hazard Mater. 357, 73–80.

Zou, H., Li, W., Liu, J., Buyukada, M., Evrendilek, F., 2020. Catalytic combustion performances, kinetics, reaction mechanisms and gas emissions of Lentinus edodes. Bioresour. Technol. 300, 122630.